Plasmon-driven Surface Functionalization of Gold Nanoparticles

M Nguyen, I Tijunelyte, C Mangeney, N Félidj

Chapter One

Plasmon-driven Surface Functionalization of Gold Nanoparticles

M. Nguyen[a,b], I. Tijunelyte[a,c], C. Mangeney[a,d] and N. Félidj[a]
[a] *Laboratoire ITODYS, Université Paris Diderot, Sorbonne Paris Cité, CNRS UMR 7086, 15 rue Jean–Antoine de Baïf, 75205 Paris Cedex 13 (France)*
[b] *School of Chemical Engineering, Hanoi University of Science and Technology, 1 Dai Co Viet road, Hanoi (Vietnam)*
[c.] *Laboratoire CSPBAT, Université Paris 13, Sorbonne Paris Cité, CNRS, UMR7244, 74 rue Marcel Cachin, 93017 Bobigny (France)*
[c] *UFR Biomédicale, UMR 8601 Université Paris Descartes Sorbonnne Paris Cité , 45 Rue des Saint Pères , 70005 Paris (France)*
Nguyenthituyetmai87@gmail.com

INTRODUCTION

Over the last decade, plasmonic nanoparticles (NPs) have been the subject of extensive research, due to their remarkable optical properties.[1, 2] These properties arise from a collective oscillation of the conductive electrons at the NP surface, under light irradiation.[3] These resonant oscillations, so-called localized surface plasmon (LSP), are mostly efficient for noble metals (gold, silver, copper), with a LSP frequency strongly dependent on the geometrical features of the NPs and the chemical nature of the metal.[4, 5] These LSP modes are characterized in the far field by an enhanced extinction mainly in the visible and near-infrared spectral region, and a strong electric field enhancement in the near-field of the NPs.[6] Therefore, plasmonic NPs

can act as a light source, as well as a heat generator and electron reservoir at the nanoscale, controllable by the light energy.[7] These outstanding properties have stimulated huge enthusiasm for the use of plasmonic NPs in medicine (hyperthermia, drug delivery, bio-imaging), surface enhanced spectroscopy or nanooptics (optical switches and modulators, plasmonic waveguides, etc.).[8-12]

In chemistry, plasmonic NPs can offer a unique platform to selectively boost the chemical reaction yields with a spatial control at the nanoscale.[13, 14] The mechanisms involved in plasmon-mediated chemical reactions result mainly from three processes: a local field enhancement, heat generation, and hot-electron transfer.[7] These processes have recently been mentioned for triggering chemical reactions. If all these examples have demonstrated the unique potential of plasmonic NPs to activate various kinds of chemical reactions, their use for plasmon-mediated chemical surface functionalization at the nanoscale has been poorly investigated so far. To address this issue and afford a selective plasmon-mediated chemical surface functionalization on gold nanoparticles, we propose two novel approaches. First one is related with combining plasmonic AuNPs as electron reservoirs and aryl diazonium salts as electron-induced surface-functionalization agents [15-17] and will be overviewed in Part 1 of this Chapter. The second approach, discussed in Part 2, involves local surface functionalization by thiols grafted via plasmon-initiated thiol-ene "click" chemistry [18].

1.1 PLASMON-INDUCED SURFACE FUNCTIONALIZATION BY DIAZONIUM SALTS

Regarding literature, aryl diazonium salts are able to bind covalently to gold surfaces via electron transfer and to form grafted polymers with thicknesses ranging from 1 nm to above 300 nm.[19-21] In first part of this Chapter, we demonstrate that plasmonic gold NPs can act as a booster to promote the grafting of diazonium derived aryl films at the gold NPs surface, in a confined nanoscale area. The aryl films derived from the diazonium salt are grafted on the gold NPs, exclusively in areas corresponding to a maximum of the near-field intensity enhancement of the gold NPs. Moreover, the grafting yield and the aryl film thickness can be monitored by the LSP wavelength as well as the energy dose produced by the incident light. Interestingly, we monitored the incident

light polarization on gold nanoparticles, to trigger plasmon excitation and obtain regiospecific local surface double-functionalization by diazonium salts. By playing on the polarization of the incident excitation light, the plasmon-driven functionalization of these isotropic NPs should result in a regioselective surface anisotropy. The plasmon-driven regioselective grafting was studied using scanning electron microscopy (SEM), atomic force microscopy (AFM), extinction micro-spectroscopy and surface-enhanced Raman spectroscopy (SERS). Calculations based on the discrete dipole approximation (DDA) method were also performed to compare the spatial localization of the functional groups around the gold nanoparticles with the electromagnetic field distribution. These approaches open way for a vast field of study on the nanoscale confinement of organic layers at the plasmonic nanostructure surface.

1.1.1 *Grafting by laser heating and Threshold energy dose E_{th}*

The laser irradiation is expected to generate a local heating, which can be sufficiently high to activate the thermal decomposition of diazonium salts and the resulting grafting of aryl layers, as described by M. Busson et al.[22] This laser induced thermal grafting could occur simultaneously with a plasmon-induced electron transfer and these two mechanisms should therefore be investigated separately to evaluate their respective efficiencies. In order to first investigate a photothermal mechanism due to laser heating at the nanostripe surface, we measured the threshold energy dose Eth, corresponding to a threshold temperature Tth above which the grafting of aryl layers could be induced photothermally, in the absence of any plasmonic excitation. The grafting by laser heating of aryl films derived from the 4-(2-hydroxyethyl)-benzene diazonium tetrafluoroborate (HEBDT) salt is demonstrated through the use of lithographically designed gold nanostripes (width W=125 ±5nm, height H=50±5nm, length L~100µm, and interparticle distance Λ~5µm) lying on an ITO coated-glass substrate.[23] Similarly, to metal NPs (a stripe can be understood as a "nanoparticle" with one infinitely extending dimension), their LSP resonance and extinction peak can be switched *on* and *off* by changing the incident polarization. [24] When the polarization of the incident illumination is perpendicular to the stripe length (transverse polarization), the observed enhanced extinction peak is

assigned to a dipolar LSP resonance, consistent with previous results.[25] In contrast, for an incident electric field parallel to the stripes (longitudinal polarization), no LSP resonance is excited, leading to an extinction spectrum with a low signal, similarly to a gold flat film. The LSP wavelength is located at λ_{LSP} ~640 nm for a transverse polarization. The gold nanostripes (GNTs) were homogeneously immersed in a solution of HEBDT (3 mM).

The threshold energy dose E_{th} was estimated using AFM, by comparing the height of a single GNT immersed in HEBDT, before and after laser irradiation with two different laser powers (P_0 = 0.089 mWμm^{-2} and P_1= 0.86 mW μm^{-2}) and by varying the irradiation time. The experiments were carried out with a longitudinal polarization, for which no LSP resonance was excited. As an example, Fig. 1a shows the profile of the cross section of a single stripe measured by AFM, before and after laser irradiation under longitudinal polarization, after 240 seconds using a power P_0=0.089 mWμm^{-2}. The height difference between the two profiles points out the grafting with a homogeneous thickness of 3 ±0.5 nm. The aryl grafting is attributed to the thermal decomposition of the diazonium salts induced by the laser heating generating aryl cations able to attach to the metallic surface. For the two laser powers, the measured thicknesses of the aryl films were reported versus the irradiation time (not shown). The aryl film thickness appears to increase with the incubation time, reaching around H_{aryl} = 4 nm after t_1 = 40s of irradiation for a laser power of P_1=0.86 mWμm^{-2} or after t_0 = 300s of irradiation for a laser power of P_0= 0.089 mWμm^{-2}. Interestingly, the aryl film thickness appears to depend exclusively on the energy dose (which represents the product of the laser power by the incubation time), deduced from the two sets of irradiation conditions (see Fig. 1b). For instance, an aryl thickness of ~4 nm is obtained for an energy dose of E= 26.5 mJ μm^{-2}. From these curves, a threshold energy dose of E_{th}= 5.5 mJμm^{-2} could be deduced, above which the laser heating is sufficient to induce the grafting of the diazonium-derived aryl film. This value is also the threshold below which the laser heating is not sufficient to induce the grafting of the aryl.

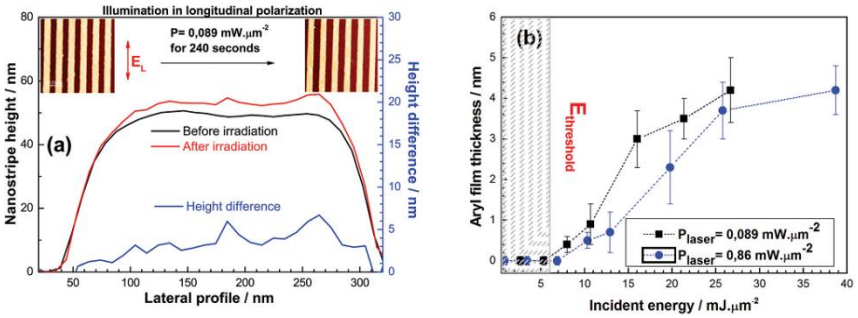

Figure 1. (a) Profiles of the lateral cross sections of a GNT, deduced from AFM measurements, in air: (black curve) before laser irradiation; (red curve) after irradiation in longitudinal polarization at 633 nm (P_0=0.089 mWµm^{-2}, 240s); (blue curve) differential cross sections deduced from the two previous profiles, evidencing the deposition of an aryl film with a thickness of ~3.5 nm. Inset: AFM image of the stripe array before and after the irradiation. (b) Aryl film thickness (deduced from AFM measurements) versus the energy dose E (mJ µm^{-2}).

1.1.2 *Plasmon-induced grafting on 1D structure arrays of gold nanostripes*

To study exclusively the plasmon-induced grafting and be sure that the laser heating is not involved in the grafting mechanism, the next step consisted of working below this threshold energy dose, but under plasmon excitation. The nanostripe array was illuminated in its LSP resonance and in transverse polarization, thus under plasmon excitation. The incident laser power was kept constant at P_0 = 0.89 mWµm^{-2}, while varying the irradiation time. A GNTs array was first considered, with a LSP resonance at λ_{LSP} at 640 nm (in water), coinciding with the laser excitation (λ_{inc}=633 nm). The sample was immersed in a HEBDT solution (3 mM) at an energy dose of 0.5×E_{th}. Fig. 2a represents a topographic AFM image of a single stripe in air, before and after irradiation in transverse polarization in the HEBDT solution. The profile of the lateral cross section, after laser irradiation, measured at the same position of the stripe before and after irradiation, and with the same non-contact tip under identical scanning conditions, clearly exhibits a larger width of the stripe (~25 nm larger), while its height slightly increases (~5 nm thicker). To confirm the assumption of a LSP-mediated grafting, the GNTs were also illuminated with a longitudinal polarization, for which no LSP excitation occurs. Under these conditions, no grafting was observed. Fig.

2b confirms this assumption as the profile of the lateral cross section of the stripe remains identical after laser irradiation (Fig. 2b). To highlight the localization of the aryl film grafted on the stripe, under transverse polarization, the profiles of the lateral cross section of the stripes, after and before irradiation, were subtracted. The resulting differential profile of the cross sections, deduced from the AFM images in Fig. 2a, is displayed in Fig. 3a, revealing two lobes of 35±5 nm oriented along the borders of the stripe. In contrast, in the case of a longitudinal polarization, the differential profile is almost flat and equal to zero (Fig. 2b and 3a).

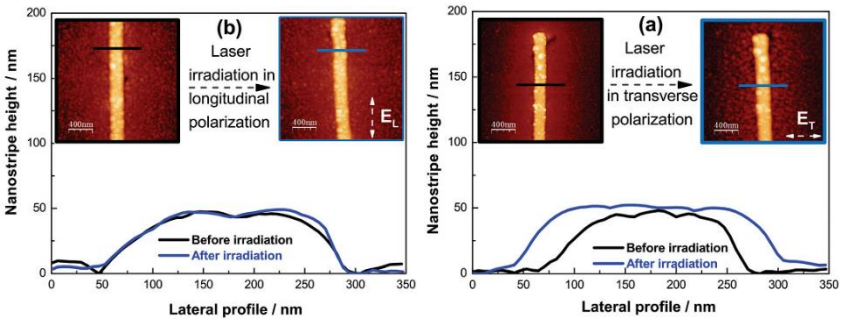

Figure 2. (a) Profiles of the lateral cross section of a single stripe (width W= 125 ±5 nm, height H= 50±2 nm, length L~100µm) deduced from the AFM images displayed in the inset: (black curve) before laser irradiation; (blue curve) after laser irradiation under transverse polarization (energy dose: E= 0.5×Eth). (b) Profiles of the lateral cross section of a single stripe deduced from the AFM images displayed in the inset: (black curve) before laser irradiation; (blue curve) after laser irradiation under longitudinal polarization (energy dose E= 0.5×Eth).

In order to elucidate the origin of the lobes appearing under LSP excitation with transverse polarization, the electric field intensity distribution around a single stripe was mapped, using the discrete dipole approximation (DDA) method.[26, 27] For calculation, we considered a gold stripe target with a width of 125 nm and height of 50 nm. The incident polarization was set perpendicular to the stripe. The interaction between the stripe and the substrate was taken into account, enabling us to make reliable comparisons between the experimental and calculated spectra. A good match was obtained between the experimental and calculated extinction spectra for the LSP wavelength (located ca. 640 nm in water) and the band shape. The optical near-field enhancement of the stripe was then calculated, using an incident

wavelength of 633 nm. Fig. 3b displays the distribution of the near-field intensity enhancement on a unit cell length of a smooth stripe target excited with a transverse polarization. The three-dimensional mapping of the optical near-field shows variations only in the cross-sectional area perpendicular to the stripe, with the stripe length remaining constant. Interestingly, the enhancement is mainly located on the side of the stripe at the ITO/glass interface, where a maximum of enhancement factor (EF) of ~1.5×10^2 (in intensity) is evidenced. In contrast, almost no enhancement is observed on top of the stripe. The remarkable agreement between the spatial confinement of the aryl grafted film (Fig. 3a) and the spatial distribution of the electromagnetic field enhancement (Fig. 3b) implies that the enhanced near-field intensity is responsible for the grafting of the diazonium-derived aryl film, under LSP excitation.[28] The aryl film grafting can be explained by the capacity of the gold nanostripes under LSP excitation to act as electron-rich reservoirs, in the area of maximum EF. This could stimulate the promotion of an electron transfer from the gold nanostripes to the diazonium salts, under LSP excitation, resulting in the formation of aryl radical species, able to bind the gold surface through covalent bonds. The aryl film grafting (~5 nm thick) observed on top of the stripe might be explained by a thermal effect, due to an increase of the temperature at the stripe surface, upon strong light absorption under LSP excitation. This increase of temperature may approach or exceed locally the threshold energy measured in the absence of LSP excitation, and can lead to the presence of the aryl film grafting on top of the gold nanostripes. It could also originate from the nanoscale surface roughness features located on top of the stripes, resulting in additional near-field enhancements randomly distributed on the stripe.

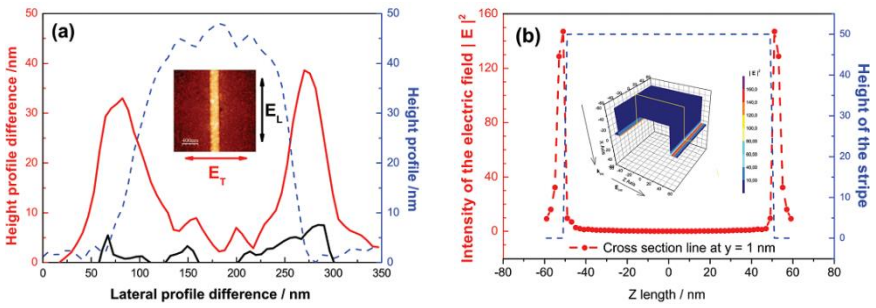

Figure 3. (a) Height profile difference of a single stripe deduced from the profile of the lateral cross section before and after irradiation displayed in Fig. 2 (λ_{exc}= 633 nm, energy dose E= 0.5×E_{th}): (red curve) for a transverse polarization; (black curve) for a longitudinal polarization. The blue dashed curve indicates the profile of the lateral cross section of the stripe before irradiation. (b) Mapping of the near-field intensity enhancement $|E|^2$ on a unit cell with a W= 125 nm wide stripe, and H= 50 nm, using the DDA method. The transverse section profile corresponding to the 3D mapping of the NF enhancement is indicated in red. The dashed blue line represents the lateral cross section of the target.

To further confirm the key role of the plasmonic excitation for the grafting of aryl films, a GNTs array presenting a LSP resonance λ_{LSP}= 530 nm (in water), far from the excitation line (λ_{inc} = 633 nm), was subjected to the same grafting experiment. After laser irradiation in transverse polarization, but without any LSP excitation (the laser is at 633 nm while the LSP is at 530 nm), the profile of the lateral cross section remains identical to the one before irradiation (data not shown). These results demonstrate the crucial role of LSP excitation in the grafting mechanism and confirm a plasmon-mediated grafting of the aryl film on the GNTs.
The influence of the energy dose upon the thickness of the aryl film and its confinement on the nanostripes was studied by varying the energy dose from 0.5×E_{th} to 3×E_{th}, under LSP excitation (see Fig. 4). Above E_{th}, the differential AFM images point out again a grafting of the aryl film mainly at the borders of the stripes, attributed to LSP excitation. In addition, an aryl film grafting significantly takes place at the center of the stripe, as shown in the inset of Fig. 4 (upper part). The higher the energy dose, the thicker the aryl film is at the center (up to H_C~15 nm at the center of the stripe for E=3×E_{th}). This grafting at the center of the stripe can be explained by a thermo-plasmonic effect, due to a strong light absorption under LSP excitation. Interestingly, the aryl film appears always thicker in transverse polarization (under LSP excitation) than in longitudinal polarization (no LSP excitation), for a fixed energy dose. The aryl film thickness at the center of the stripe is H_C~14 nm for a transverse polarization (the inset of Fig. 4, upper part), while in longitudinal polarization, H_C is only ~3 nm at the center of the stripe (the inset of Fig. 4, lower part). These results highlight two grafting mechanisms occurring at the same time. When the energy dose is superior to the threshold energy, the thermally induced grafting, under laser heating, occurs all along the gold nanostripes, regardless of the

polarization, transverse or longitudinal. In addition to the deposition of aryl layers within the area of high field enhancement under LSP excitation (leading to the formation of the lobes described above), the increase of temperature at the stripe surface caused by LSP excitation, may significantly contribute to the aryl film grafting at the center of the stripe, above the threshold energy dose.[29] As a consequence of LSP excitation, the threshold energy above which the aryl film grafting takes place has been lowered to a new threshold value of E_{th}^{LSP} = 1.3 mJ.µm^{-2}, as illustrated in Fig. 4.

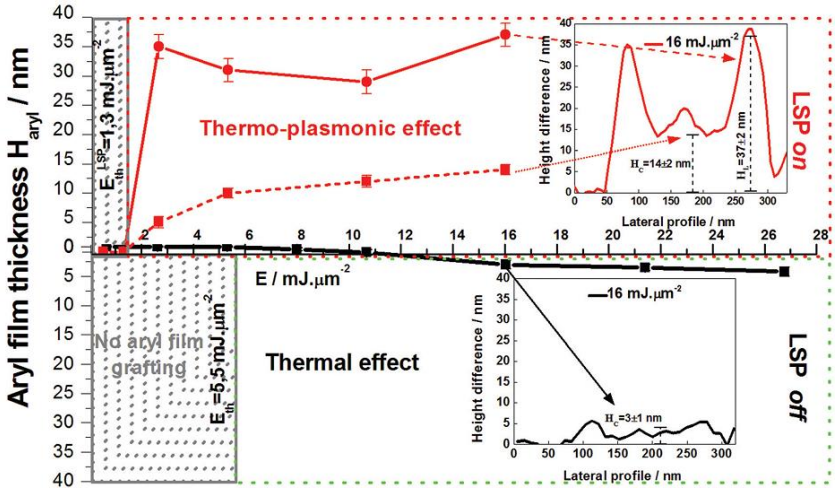

Figure 4. Aryl layer thickness grafted on a GNT (measured by AFM) versus the incident energy dose E (mJµm^{-2}). The black squares represent the aryl layer thickness after laser irradiation at various energies with a longitudinal polarization (no LSP excitation takes place). The red squares and red circles represent the aryl layer heights H_C and H_L measured at the center and the borders of a single stripe, respectively, after laser irradiation at various energies with a transverse polarization (under LSP excitation). The threshold energy below which aryl film grafting doesn't take place is lowered, from E_{th}= 5.5 mJµm^{-2} under off LSP excitation, to a new threshold value of E_{th}^{LSP}= 1.3 mJµm^{-2} under LSP excitation.

In summary, a plasmon-mediated grafting of aryl films derived from diazonium salts on regular arrays of gold nanostripes was demonstrated. This grafting occurs specifically in the regions of maximum of field enhancement.

1.1.3 *Plasmon-driven grafting on 2D structure array of gold nanorods*

1.1.3.1 *Description of the gold nanorods array*

Lithographic gold nanorods (GNRs) arrays (diameter D = 100 ± 5 nm, length L = 165 ± 5 nm, height H = 47 ± 3 nm, interparticle distance Λ ~ 300 ± 5 nm) were elaborated on an indium–tin-oxide (ITO) coated-glass substrate by electron-beam lithography (EBL).[30] A representative SEM image of the array of GNRs is displayed in Fig. 5a. Due to their anisotropic shape, they display two separate surface plasmon resonance (SPR) bands corresponding to their width and length, known as the transverse and longitudinal plasmon bands. Indeed, the longitudinal LSPR mode is associated with the electron oscillations along the length axis for an incident polarization parallel to this axis. The transverse LSPR mode is associated with the electron oscillations along the short axis for a polarization parallel to the short axis of the GNRs.[12] Therefore, the transverse LSPR is located at about 560 nm while the longitudinal LSPR is at approximately 780 nm as shown in Fig. 5b (the spectra are recorded in water).

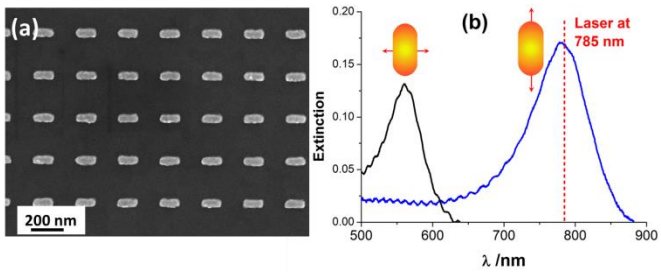

Figure 5. Characterization of the GNRs array. (a) SEM image; (b) Extinction spectra under transversal (black curve) and longitudinal polarization (blue curve) in water.

1.1.3.2 *Plasmon-driven grafting on gold nanorods array*

The GNRs arrays were then homogeneously immersed in the solution of the HEBDT salt (3 mM) and illuminated by a laser, during 10s. A Krypton laser at 785 nm was used since its wavelength matches the maximum of extinction of the longitudinal LSPR band. This excitation

wavelength has been selected for the plasmon-induced grafting of poly(aryl) films, since a strong field enhancement at the extremities of the rods is expected, provided that the incident polarization is set parallel to the long axis of the rod. The aryl film grafting is thus expected to be particularly efficient under such experimental conditions. The incident polarization was set parallel to the AuNRs long axis. It is worth mentioning that the laser heating induces the grafting reaction by itself, even in the absence of any plasmon excitation, when the exposure energy dose exceeds a given threshold E_{th}, as shown in a previous part. In the case of thermal grafting, the layers are observed all around the nanoparticles, with a uniform distribution. Therefore, an exposure dose below this threshold value, corresponding to E=50% E_{th}, was used here to avoid side reactions by laser heating and guarantee that the grafting of poly(aryl) layers on the nanostructures was solely induced by plasmon excitation. The hybrid nanostructures, obtained before and after plasmon-mediated functionalization by the diazonium salt, were characterized using AFM (see Fig. 6 a,b). An elongation of the nanoparticles of ca. 40 nm is observed along the long axis after plasmon-induced grafting. To visualize the spatial extent of the grafted layers around the nanorods, AFM profiles of the nanoarrays before and after plasmon-induced grafting were recorded and subtracted. From these profiles and the subtraction between the AFM images, displayed in Fig. 6 c-e, it appears that the grafting of the poly(aryl) layers is highly confined at each end of the nanorod long axis and that no grafting occurs on top of the nanoparticles. However, the grafting of nanoscale poly(aryl) layers is not strictly confined to each ends of the nanorods as shown by the

AFM profiles recorded along the short axis direction. Indeed, they reveals that poly(aryl) layers are also grafted along each side of the nanorods with an enlargement of ca. 10 nm of the hybrid nanoparticle along the short axis direction. This is due to the spatial extension of the electromagnetic field enhancement away from the irradiation polarization axis leading to a poly(aryl) film, which is not strictly confined along the long axis, but slightly spread out towards the short axis.

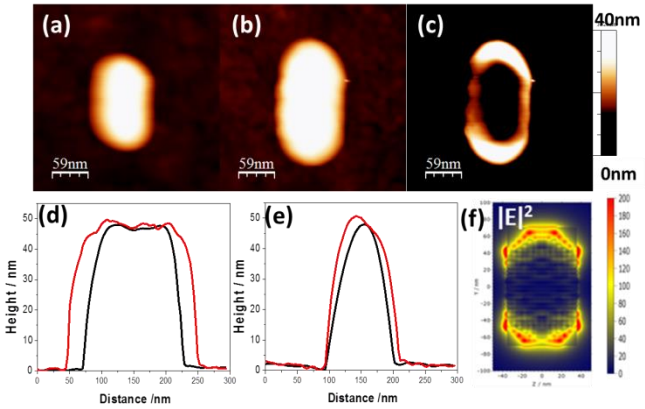

Figure 6. Snapshot of the hybrid NPs obtained after plasmon-induced functionalization. (a) AFM image of a AuNR before functionalization; (b) AFM image obtained after plasmon-induced grafting along the long axis; (c) Result of the subtraction between the AFM images (b) - (a); (d,e) AFM lateral cross section profiles along the long axis (d) and short axis (e), before (black curves) and after (red curves) plasmon-induced grafting using a laser at λ_{inc}=785 nm, polarized along the long axis of the nanorods. (f) Cross-sectional view of the intensity of the electric field distribution around a rectangular rod with rounded edges thick=45nm, length=140nm, width=70nm, over a 350x175nm² ITO slab in water at 850nm.

A snapshot of the grafted poly(aryl) layers obtained after plasmon-induced functionalization was obtained by subtracting the AFM images all along the nanorods (see Fig. 6c). In order to elucidate the mechanism of the aryl film grafting appearing under LSP excitation with longitudinal polarization, the electric field intensity distribution around a single rod was mapped, using the discrete dipole approximation (DDA) method (see Fig. 6f). These calculations show that the plasmon

excitation generates enhanced electromagnetic fields, maximum at the tips of the rod. Interestingly, the spatial grafting of the poly(aryl) layers determined by AFM correlates perfectly well with the dipolar near-field intensity calculated around the GNRs. The remarkable agreement between the spatial confinement of the aryl grafted film (Fig. 6c) and the spatial distribution of the electromagnetic field enhancement (Fig. 6f) implies that the enhanced near-field intensity is responsible for the grafting of the diazonium-derived aryl film, under LSP excitation. Therefore, the aryl film grafting can be explained by the capacity of the gold nanorods under LSP excitation to act as electron-rich reservoirs, in the area of maximum electric field. The LSP resonance and extinction peaks can be switched on and off by changing the incident polarization. Therefore, when the polarization of the 785 nm laser was turned along the short nanorod axis, no grafting could be detected as revealed by the AFM profiles (not shown). As the plasmon is not excited in this configuration, this experiment can be regarded as a control test to highlight the role of the plasmon excitation in the functionalization of the GNRs.

In summary, we have shown the ability to modify locally the surface chemical properties of gold nanorods by plasmon-mediated grafting of functional poly(aryl) layers. This anisotropic functionalization strategy is triggered by the site-selective electron mediated reduction of aryl diazonium salts, depending on the polarization of the incident illumination.

1.1.4 *Plasmon-driven multi-functionalization of gold nanodisks array*

The strategies developed so far provided a single functionalization of the surface with only one type of organic layer grafted in nanoscale region. Extension of these strategies to the multi-functionalization of surfaces represents a major breakthrough in plasmon-mediated chemistry, in order to achieve the grafting of various chemical groups in distinct nanoscale regions. We address this issue in this part by monitoring the incident light polarization on gold nanodisks, to trigger plasmon excitation and obtain regiospecific local surface double-functionalization by diazonium salts (see Fig. 7).

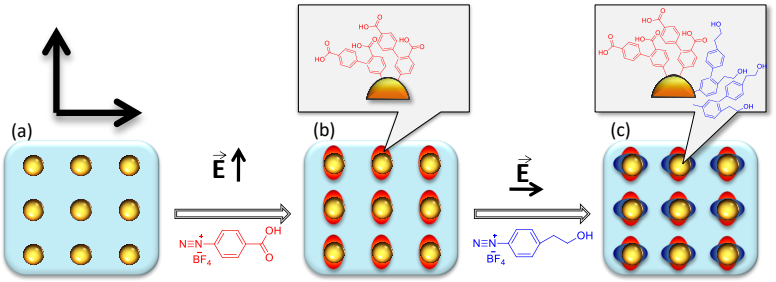

Figure 7. Scheme of the regioselective multifunctionalization of GNDs under plasmon excitation with polarized light. The nanostructures were first incubated for 180s in an aqueous solution of carboxy-phenyl diazonium salt (3 mM) under laser irradiation polarized in Y direction. Then, the nanostructures were incubated for 180 s in an aqueous solution containing a hydroxy-ethyl phenyl diazonium salt (3 mM) under laser irradiation, polarized in X direction.

Lithographic gold nanodisks (GNDs), with no capping agents on their surface, were chosen for the proof of concept, as they display a symmetric geometry in the XY plane and a uniform surface chemistry. GNDs arrays (diameter D = 100 ± 5 nm, height H = 50 ± 5 nm, interparticle distance Λ = 300 nm) were elaborated ITO coated-glass substrates by EBL. The optical response of the nanodisks demonstrates the main peak at 655 nm which represents the LSPR dipolar mode in aqueous solution. By playing on the polarization of the incident excitation light, the plasmon-driven functionalization of these isotropic NPs should result in a regioselective surface anisotropy. Functionalization agents based on aryl diazonium salts were selected as they were shown in the previous part to graft on Au nanostripes through plasmon-induced electron transfer. In this part, two types of aryl diazonium salts were used, bearing either hydroxyl (4-hydroxyethyl benzene diazonium tetrafluoroborate), or carboxyl-terminated groups (4-carboxy-benzene diazonium tetrafluoroborate). This plasmon-mediated multi-functionalization approach opens promising perspectives for the elaboration of nanostructured surfaces with chemical anisotropy.

In order to demonstrate that the LSPR excitation can locally trigger regiospecific surface functionalization, the GNDs arrays were homogeneously immersed in the solution of carboxy-terminated diazonium salts (3 mM) and illuminated by a laser polarized along the Y

axis, during 180 s. The optical exposure was performed under normal incidence, and the He–Ne laser (λ_{inc} = 633 nm) was focused on the nano-array through a microscope objective (×10 numerical aperture N.A. #0.25), resulting in a circular laser spot of ~ 5 µm diameter at the surface. The incident wavelength λ_{inc}= 633 nm of the laser excitation matches well the LSPR of the gold nanodisk (λ_{max}= 655 nm). It is worth mentioning that laser heating induces the grafting reaction, probably through a cationic pathway, when the exposure energy dose exceeds a given threshold E_{th}, even in the absence of any plasmon excitation, as shown in a previous part. In the case of thermal grafting, the layers are observed all around the nanoparticles, with a uniform distribution. Therefore, an exposure dose below this threshold value, corresponding to E = 50% E_{th}, was used here to avoid side reactions by laser heating and guarantees that the grafting of poly(aryl) layers on the nanostructures was solely induced by LSPR excitation. The obtained hybrid nanostructures were characterized by SEM as the metallic NPs and the poly(aryl) layers show different contrasts (Fig. 8a). Polymer lobes can be visualized easily along the Y-axis in the vicinity of the nanodisks. In order to verify that the plasmon-induced grafting occurs specifically in the regions of maximum of field enhancement, the mapping of the intensity of the electric field around the nanodisks was calculated by the DDA (see Fig. 8b). It evidences a strong amplification on each side of the nanodisk along the excitation axis with a progressive attenuation away from the axis. From the comparison of the spatial extent of the grafted layers in the XY plane, observed by SEM, it is clear that the regioselective grafting of the poly(aryl) layers is a polymer replica of the dipolar near-field intensity.

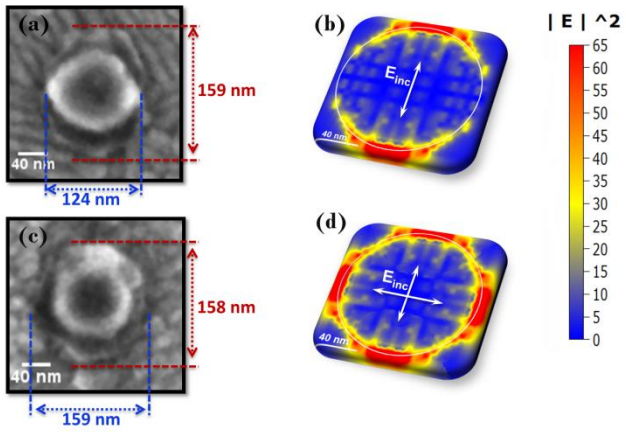

Figure 8. SEM images of a single nanopartilce after plasmon-induced grafting of (a) carboxyphenyl layers along the Y direction and (c) additional hydroxyethyl phenyl layers along the X axis. Irradiation conditions: λ_{inc} = 633 nm, 180s with a power of P=0.8 mW μm^{-2}. Mapping of the near-field intensity enhancement $|E|^2$ upon irradiation along the Y axis (b) and both X and Y axis (d), on a unit cell with a nanodisk of 100 nm diameter, H = 50 nm, using the DDA method.

The extension of the poly(aryl) layers along the Z direction (perpendicular to the nanoarray plane) was studied by AFM. The differential AFM profiles of the lateral cross sections (corresponding to the subtraction of the profiles obtained before and after plasmon-induced grafting) revealed no grafting on top of the disk and confirmed the confinement of the grafted layers only in the X-Y plane, on each sides of the GNDs (Fig. 9a). The SERS spectra, recorded after plasmon-induced grafting, looked very similar to those obtained after spontaneous reaction apart from an enhancement of the shoulder at 1614 cm-1, at the higher frequency side of the aromatic ortho-meta C=C bond vibration band (not shown). The main Raman band at 1586 cm-1 can be assigned to the aromatic ring deformations in the first layer grafted onto the gold surface, whereas the shoulder at 1614 cm-1 corresponds to the same vibration in the poly(aryl) layer above, covalently linked to the former. The intensity increase of this shoulder thus confirms the polymeric nature of the grafted organic layer. Interestingly, strong variations of the SERS signal intensity were observed depending on the incident

polarization. The spectra recorded in the Y direction, matching the polarization of plasmon-induced grafting, gave the highest SERS signal intensities. Nevertheless, the SERS signal is not fully switched off along the X direction, perpendicular to the polarization of plasmon-induced grafting. This is due to the spatial extension of the electromagnetic field enhancement away from the irradiation polarization axis leading to a poly(aryl) film, which is not strictly confined along the Y axis, but slightly spread out towards the X-axis (Fig 8b).

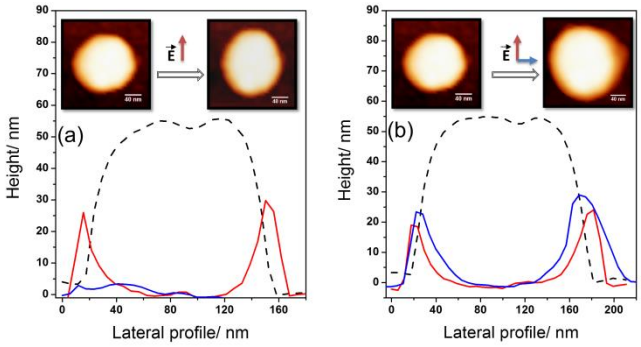

Figure 9. (a) Plasmon-induced grafting of the first carboxy-aryl layer, using an incident polarization along Y axis. Top: AFM image of a single disk before (left) and after (right) plasmon-induced grafting along Y axis. Bottom: Lateral cross section profile along Y axis after grafting (dashed line) and differential lateral cross section along Y axis (red line) revealing two main lobes along the Y direction and along X (blue line) confirming no grafting along X direction. (b) Plasmon-induced grafting of the second hydroxyethyl-aryl layer, using an incident polarization along X axis. Top: AFM image of a single disk before grafting (left) and after double plasmon-induced grafting along Y and X axis (right). Bottom: Lateral cross section profile along X axis after grafting (dashed line) and differential lateral cross section along Y axis (red curve) and X axis (blue curve) revealing two main lobes along the Y and X directions.

In a second step, the samples were thoroughly cleaned with ethanol and dried before a new immersion in an aqueous solution of the other diazonium salt, hydroxyethyl benzene diazonium. A second exposure with the same energy dose but an incident polarization oriented along the X-axis was then performed. Fig. 8c shows the SEM image of the nanodisks after the second grafting step along the X-axis. New polymer nodules are observed on each side of the gold nanodisks along the X direction. On the basis of the SEM images recorded at both steps, it turns

out that the two different poly(aryl) layers, bearing either carboxyl or hydroxyethyl substituents, were selectively integrated in different orientations around the gold nanodisks via near-field plasmonic excitation.

The AFM differential profile of the single disk before and after the two-step grafting (Fig. 9b) evidences the bi-directional anchoring of the poly(aryl) nanolayers, which perfectly matches the electric field distribution around the nanodisks, according to DDA calculations (Fig. 8d). Note that the corresponding optical and SERS spectra also confirm this bi-directional anchoring (data not shown).

The influence of the energy dose upon the spatial extent of the poly(aryl) nodules along the Y and X direction was further estimated by SEM. Figure 10 displays the elongation observed in Y and X direction. It reveals two important features:

- The growth of the poly(aryl) layer with the energy dose is directional along the excitation polarization axis. Indeed, the elongation along Y increases with the energy dose when the excitation is polarized along the Y axis, while the elongation along the X axis remains constant, and inversely for the X polarization.
- The thickness of the grafted layers increases with the energy dose, until reaching ca. 40-60 nm, depending on the diazonium salt: the carboxyphenyl-derived layers appear slightly thicker than the hydroxyethyl ones.

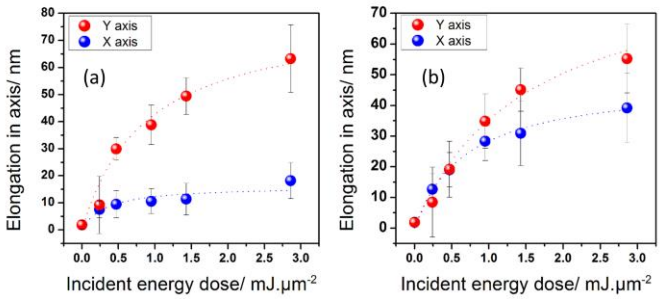

Figure 10. Plot of the thickness (measured by SEM) of the grafted poly(aryl) layer along the Y and X direction, as a function of the incident energy dose from 0 to 3 $mJ.\mu m^{-2}$, (a) after plasmon-induced first carboxy-aryl layer grafting along Y and (b) after second hydroxyethyl-aryl layer grafting along X.

The influence of the incident energy dose upon the growth of the carboxy-terminated poly(aryl) layer was also controlled by SERS. The ratio of the relative intensities I_{1614}/I_{1586} of the two bands at 1614 and 1586 cm^{-1}, assigned respectively to the aromatic ring deformations in the poly(aryl) layer and in the first layer directly grafted on gold via Au-C bonds was plotted against the dose (see Fig. 11).

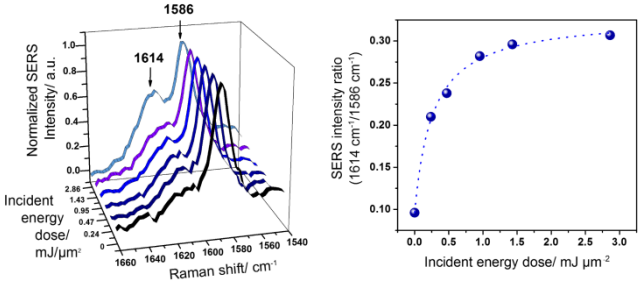

Figure 11. (a) SERS spectra in the 1540-1660 cm^{-1} region, recorded on the nanodisk arrays after plasmon-induced grafting of carboxy-phenyl layers along the Y direction; (b) Plot of the I1614/I1586 SERS intensity ratio as a function of the incident energy dose from 0 to 3 $mJ.\mu m^{-2}$.

An increase in the energy dose leads to a clear enhancement of the shoulder at 1614 cm^{-1}, revealing the growth of the poly(aryl) layer. Although the SEM analysis indicates a continuous thickening of the poly(aryl) layers upon an increase of the incident energy dose, the I_{1614}/I_{1586} SERS ratio reaches a plateau value at around 1 $mJ.\mu m^{-2}$, revealing the maximum distance from the nanostructure's surface probed by SERS. This energy dose corresponds to a poly(aryl) thickness of ca. 40 nm, as shown in Fig. 10, above which the additional poly(aryl) layers grafted on the gold nanodisks are no longer detected by SERS. Note that this distance correlates perfectly well with the spatial extent of the electromagnetic field, calculated by DDA. It is therefore possible to use this plasmon-mediated functionalization approach to probe the distance-dependence enhancement effect of SERS in hot spot regions. Moreover, it is an efficient way to modify only the regions of high electromagnetic field whilst leaving the other area of the nanoparticle surface chemically passive.

In summary, we have shown that it is possible to pattern the surface chemical properties of plasmonic gold nanodisks by two different types of functional poly(aryl) layers, bearing either carboxyl or hydroxyethyl

pendant groups. This double-functionalization strategy is triggered by the polarization of the incident illumination leading to a site-selective hot-electrons mediated reduction of aryl diazonium salts.

1.1.5 *Conclusion*

Compared to conventional grafting methods, the approach described in this chapter offers several advantages: (i) it is very fast (it occurs in a few seconds upon laser irradiation, while the usual spontaneous methods require several hours); (ii) it gives thick poly(aryl) layers (up to 40-60 nm) using low diazonium salt concentrations; (iii) the grafting takes place selectively in the regions of maximum of field enhancement, in contrast to the homogeneous coating obtained under spontaneous grafting. This plasmon-mediated functionalization approach therefore opens promising prospects for the nanoscale confinement of organic layers at the gold nanoparticles surface. It could also provide a general strategy to attach molecules to hot spot regions and further improve their detection for (bio)sensing applications, using Surface-Enhanced Raman Spectroscopy.

1.2 PLASMON-INITIATED SURFACE FUNCTIONALIZATION BY THIOL-ENE "CLICK" CHEMISTRY

Thiol-ene coupling reaction is one of the "click" chemistry processes and described as simple method which is modular, widely scoped and generating high yields. This reaction consists in grafting thiol-bearing molecules to a carbon double bond. It had a significant impact in polymer synthesis and material science [31, 32] and recently has attracted considerable interest in surface functionalization and modifications.[33, 34]

By means of conventional approach thiol-ene reaction is performed through UV light or thermal activation, with the presence of a radical initiator. In this part of the Chapter, we will demonstrate that the thiol-ene coupling can be locally triggered using the visible range light source and by exploiting nanoplasmonic effects. The kinetics of this reaction was monitored in situ by Surface Enhanced Raman Scattering (SERS). After investigating the reaction rates on different diameters of gold nanocylinders (NCs) made by electron-beam lithography (EBL) we show

that the reaction can be tuned by controlling the NCs plasmonic properties.

1.2.1 *Fabrication of substrates*

Arrays of gold nano-cylinder (NCs) on glass were produced by electron beam lithography and lift-off techniques [35, 36] and were designed to contain the variable diameters of NCs: 110 nm, 140 nm and 200 nm (electron microscope micrograph can be seen in Fig. 12a). EBL technique is known to allow the good control of the size and shape of the nanostructures. Thus, the substrates ensure the reproducibility of LSPR position and SERS signal. The height of the NCs was set to 60 nm where gold was evaporated on 3 nm of chromium (Fig. 12b) for better adhesion. The gap between two NCs was set at 200 nm (side to side) in order to avoid any near-field coupling effects.

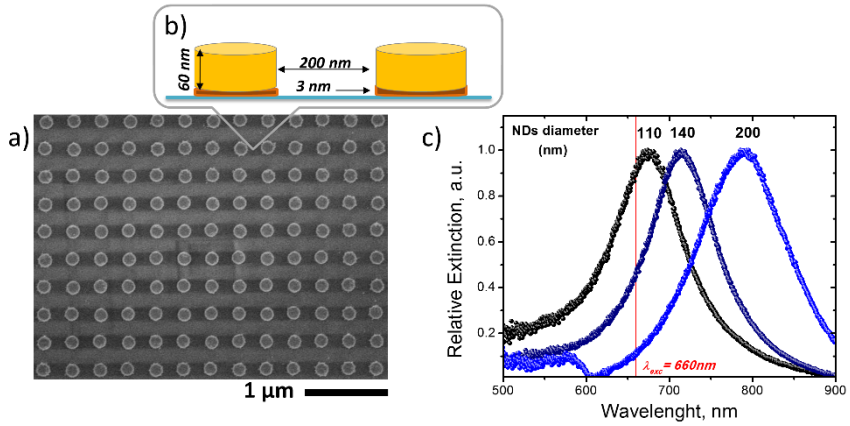

Figure 12. a) Scanning electron microscopy image of an array of NCs with a diameter of 200 nm. b) Scheme of the nanocylinders (NCs) used in the experiments. e) Extinction spectroscopy measurements in water on 110 nm (black curve), 140 nm (dar blue curve) and 200 nm (blue curve) NCs arrays. The red line indicates the laser wavelength used for thiol-ene reaction initiation and SERS investigation.

Fig. 12c demonstrates the extinction spectra of fabricated NCs in aqueous environment. LSPR position of the 110 nm diameter NCs array was observed close to 660 nm (as excitation laser wavelength used to

initiate the reaction), whereas 140 nm and 200 nm NCs had a LSPR position red-shifted or nearly out of resonance, respectively.

1.2.2 *In situ thiol-ene click reaction*

Thiol-ene "click" reaction implicates the addition of a thiol to an alkene function via a free-radical mechanism [37] (Fig. 13).

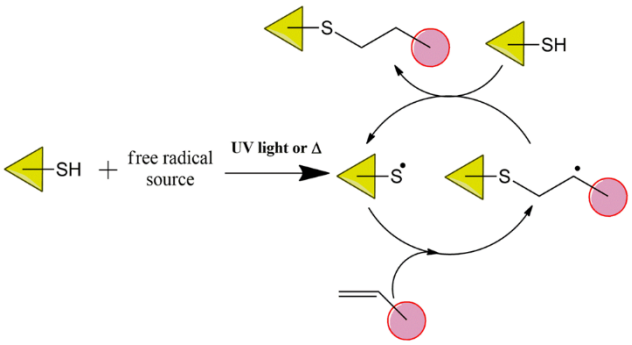

Figure 13: Schematic illustration of the free-radical thiol–ene coupling mechanism.

Briefly, first thiol group is converted to a thiyl radical thanks to the interaction with a free radical initiator exposed to UV light or to a specific temperature [38]. Active thiyl radical react then with the alkene group and forms a carbon centered radical. From here the reaction turns to a propagation step resulting in the formation of thio ether as a reaction product and a new thiyl radical which then subsequently is involved in the reaction chain.

Herein, thiol-ene "click" reaction was carried on plasmonic substrates pre-functionalized by allyl mercaptan using 2,2′-Azobis(2-methylpropionamidine) dihydrochloride (AAPH) as free radical initiator and thiophenol as reactant (scheme of reaction can be seen in Fig. 14a). Regarding literature, the AAPH can be decomposed into cationic radicals under exposition to UV light (365 nm) or temperature above 60 °C. In our case, the local reaction at the nanoscale level was initiated on the surface of the gold NCs in aqueous environment using a laser excitation wavelength of 660 nm. The laser beam was focused on the sample with a 60x objective (N.A. 0.7).

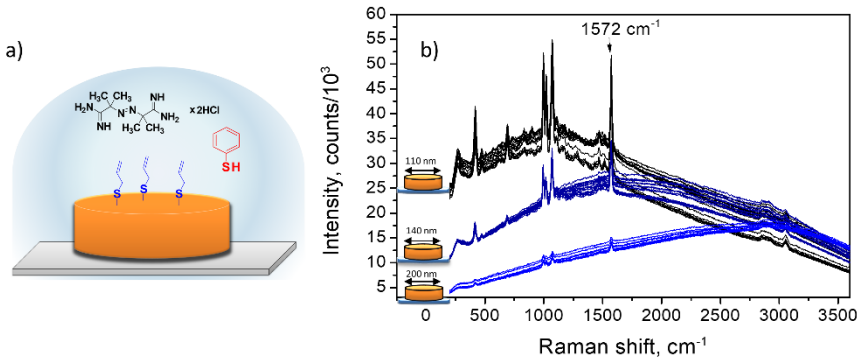

Figure 14. a) Scheme of the thiol-ene reaction configuration. b) SERS spectra of grafted thiophenol onto gold NCs of 110 nm (black spectra), 140 nm (dark blue spectra) and 200 nm (blue spectra) diameter.

The reaction kinetics was monitored by SERS in real time using the same laser beam. SERS spectra were first recorded on the 110 nm NCs for 30 min and the process was then reproduced on the NCs of 140 nm and finally on the NCs of 200 nm.

Obtained SERS spectra for different arrays of NCs can be seen in figure 14b). The peaks observed in the SERS spectra correspond to the thiophenol signal. In order to follow the kinetics of reaction, the intensity of the peak at 1572 cm^{-1} (assigned to an aromatic C=C vibration) was plotted versus reaction time (Fig. 15a) for each NCs array. One can notice that the observed SERS intensity of the thiophenol peak increases with the time and saturates in less than 10 min for the 110 nm and the 140 nm diameters NCs. Time needed to complete local thiol-ene coupling reaction was very fast while in literature it has been estimated to be in the range of several hours using normal conditions [39] (i.e. without NCs and using UV excitation). Worth mentioning, that the saturation of thiol-ene process even after 40 min was not reached for the 200 nm diameter NCs.

To determine precisely the reaction time, the obtained experimental data were fitted with a first order Langmuir isotherm:

$$\theta = \theta_{sat}\left[1 - exp^{\left(-\frac{t}{\tau}\right)}\right] \quad (1)$$

where θ is the surface coverage, θ_{sat} is the saturation of the coverage, t is the time and τ is the reaction time constant.

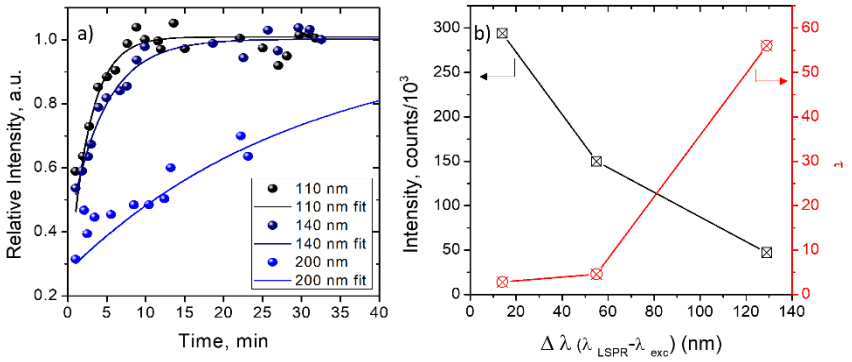

Figure 15: a) Relative SERS intensities of the thiophenol peak at 1572 cm^{-1} versus reaction time for the 110 nm (black dot), 140 nm (dark blue dot) and 200 nm (blue dot) diameter NCs. Solid lines are the fitting using the equation (1) (110 nm: black line, 140 nm: dark blue line and 200 nm: blue line). b) Absolute SERS intensity of the peak at 1572 cm^{-1} at saturation point and reaction time constant plotted versus the mismatch between the LSPR position of NCs and the used laser excitation wavelength.

Fig. 15b demonstrates the absolute SERS intensity and the reaction time constant, τ (time required to reach 63% of SERS signal saturation) versus the mismatch between the LSPR position of NCs and the laser excitation wavelength, $\Delta\lambda=\lambda_{LSPR}-\lambda_{exc}$. One can notice that the reaction time is strongly dependent on the LSPR position of different diameters NCs. A twenty times faster reaction was witnessed on highly resonant 110 nm NCs compared to 200 nm NCs. Unexpected result was achieved for 140 nm diameter NCs which have a 54 nm difference between the its LSPR position and the excitation wavelength. In this case just slightly lower reaction efficiency was obtained compared to the one measured on 110 nm NCs.

The obtained results are not straightforward because grafting of thiophenol on the NCs can be governed by two other parallel mechanisms. Firstly, from the literature it is known that short thiol bearing molecules (like allyl mercaptan in this case) form non-homogeneous self-assembled monolayer (SAM) due to the lack of intermolecular interactions [40]. Thus, non-blocked active gold sites can be available for spontaneous thiophenol grafting. Secondly, a

competitive molecular replacement of grafted allyl mercaptan by thiophenol could take a place directly on the gold surface [41]. Therefore, the SERS signal achieved during the thiol-ene experiments could then also include probable contributions from these two competitive thiophenol direct interactions with the NCs surface.

To address latter concern and to prove that achieved experimental results actually correspond to the thiol-ene "click" process, three different experimental conditions were tested as a negative controls, including: (i) a duplication of the thiol-ene reaction excluding a radical initiator, (ii) testing reaction on mercaptoethanol functionalized NCs to monitor the competitive molecular displacement by thiophenol and (iii) observing the rate of direct thiophenol grafting to non-functionalized gold NCs surface.

Two first negative control samples indicate low rate replacement of short thiols previously deposited on the NCs by thiophenol. Moreover, the obtained SERS signal was nearly constant with time and considerably lower than the one recorded during the thiol-ene reaction [18]. On another hand, results obtained from third negative control sample, where the kinetics of thiophenol SAM formation was monitored, gave a base for useful comparison with thiol-ene reaction sample. First of all, it was revealed that the rate of thiophenol attachment by thiol-ene process is faster than the one of spontaneous grafting, suggesting the strong impact of the "click" chemistry process. Secondly, the SERS signal for 110 nm diameter NCs on both samples was equivalent at the saturation point, meaning that the same NCs coverage is reached using either the thiol-ene reaction or the simple SAM formation.

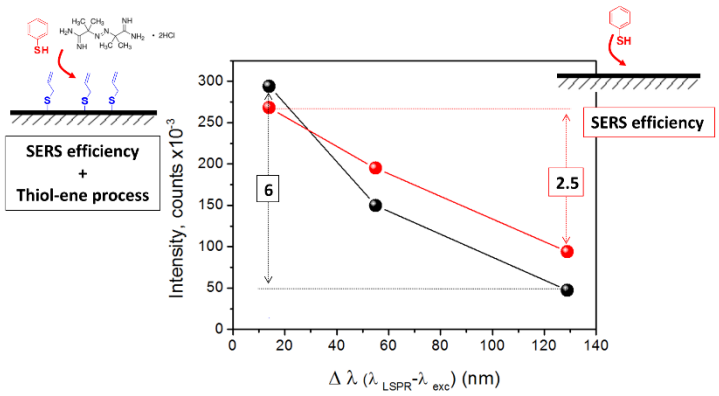

Figure 16: Absolute SERS intensity of the peak at 1572 cm^{-1} at saturation point plotted versus the mismatch between the LSPR position of NCs and the used laser excitation wavelength for thiol-ene reaction (black spheres) and thiophenol spontaneous SAM formation (red spheres).

Thiophenol SAM formation is not dependent on the plasmonic properties of the NCs since the thiol interaction with gold is not thermally or optically activated. Thus, to demonstrate the plasmon contribution to the thiol-ene reaction initiation we compared the absolute SERS intensities at the saturation points for both samples (Fig. 16). In the case of thiophenol SAM formation, the SERS signal on 110 nm diameter NCs is 2.5 higher than the one measured on the 200 nm NCs and can be attributed to plasmonic effects on the SERS signal enhancement. While for the thiol-ene "click" reaction, intensity ratio was close to 6. Such a large ratio is strong evidence that radical reaction is plasmon-induced on highly resonant NCs while less efficient for the NCs with the LSPR out of resonant.

1.2.3 *Conclusion*

The results discussed in this part of the Chapter demonstrate that the thiol-ene "click" reaction which by conventional means takes several hours to be completed under specific conditions (UV light or temperature) can be successfully triggered at the nanoscale range of the gold surface by exploiting the plasmonic properties of the nanostructures. Moreover, it was showed that local surface

functionalization by plasmon-initiated thiol-ene reaction is performed in a few minutes on highly resonant nanoparticles and thus can be modulated and controlled by tuning the LSPR position.

REFERENCES

1. Kawata, S. (2007) *Nanophotonics with Surface Plasmons*. (Elsevier, Amsterdam)
2. Lal, S., Clare, S. E., andHalas, N. J. (2008). Nanoshell-Enabled Photothermal Cancer Therapy: Impending Clinical Impact*, Accounts of Chemical Research*, **41,** pp. 1842-1851.
3. Maier, S. A. (2007) *Plasmonics: Fundamentals and Applications*. (Springer US,
4. Felidj, N. (2008). Multipolar surface plasmon peaks on gold nanotriangles*, J Chem Phys*, **128,** pp. 094702-094705.
5. Becker, J. (2010). The Optimal Aspect Ratio of Gold Nanorods for Plasmonic Bio-sensing*, Plasmonics*, **5,** pp. 161-167.
6. Encai Hao, G. C. S. (2004). Electromagnetic fields around silver nanoparticles and dimers*, The Journal of Chemical Physics*, **120,** pp. 357.
7. Baffou, G. andQuidant, R. (2014). Nanoplasmonics for chemistry*, Chemical Society Reviews*, **43,** pp. 3898-3907.
8. Urban, A. S. (2011). Single-Step Injection of Gold Nanoparticles through Phospholipid Membranes*, ACS Nano*, **5,** pp. 3585-3590.
9. Moskovits, M. (1985). Surface-enhanced spectroscopy*, Reviews of Modern Physics*, **57,** pp. 783-826.
10. Häfele, V. (2015). Local refractive index sensitivity of gold nanodisks*, Optics Express*, **23,** pp. 10293-10300.
11. Pelton, M., Aizpurua, J., andBryant, G. (2008). Metal-nanoparticle plasmonics*, Laser & Photonics Reviews*, **2,** pp. 136-159.
12. Pérez-Juste, J. (2005). Gold nanorods: Synthesis, characterization and applications*, Coordination Chemistry Reviews*, **249,** pp. 1870-1901.
13. Volpe, G. (2012). Near-Field Mapping of Plasmonic Antennas by Multiphoton Absorption in Poly(methyl methacrylate)*, Nano Letters*, **12,** pp. 4864-4868.
14. Gruber, C. (2015). Imaging nanowire plasmon modes with two-photon polymerization*, Applied Physics Letters*, **106,** pp. 081101.
15. Tijunelyte, I. (2018). Multi-functionalization of lithographically designed gold nanodisks by plasmon-mediated reduction of aryl diazonium salts*, Nanoscale Horizons*.
16. Nguyen, M. (2017). Regioselective surface functionalization of lithographically designed gold nanorods by plasmon-mediated reduction of aryl diazonium salts*, Chemical Communications*, **53,** pp. 11364-11367.

17. Nguyen, M. (2016). Plasmon-mediated chemical surface functionalization at the nanoscale*, Nanoscale*, **8,** pp. 8633-8640.
18. Tijunelyte, I. (2016). Nanoplasmonics tuned "click chemistry"*, Nanoscale*, **8,** pp. 7105-7112.
19. Gehan, H. (2011). Design and Optical Properties of Active Polymer-Coated Plasmonic Nanostructures*, The Journal of Physical Chemistry Letters*, **2,** pp. 926-931.
20. Gehan, H. (2010). A General Approach Combining Diazonium Salts and Click Chemistries for Gold Surface Functionalization by Nanoparticle Assemblies*, Langmuir*, **26,** pp. 3975-3980.
21. Nguyen, M. (2015). Engineering Thermoswitchable Lithographic Hybrid Gold Nanorods as Plasmonic Devices for Sensing and Active Plasmonics Applications*, ACS Photonics*, **2,** pp. 1199-1208.
22. Ahmad, R. (2014). Tailoring the Surface Chemistry of Gold Nanorods through Au–C/Ag–C Covalent Bonds Using Aryl Diazonium Salts*, The Journal of Physical Chemistry C*, **118,** pp. 19098-19105.
23. Hohenau, A. (2006). Electron beam lithography, a helpful tool for nanooptics*, Microelectronic Engineering*, **83,** pp. 1464-1467.
24. Sow, I. (2013). Revisiting Surface-Enhanced Raman Scattering on Realistic Lithographic Gold Nanostripes*, The Journal of Physical Chemistry C*, **117,** pp. 25650-25658.
25. G. Schider, J. R. K., W. Gotschy, B. Lamprecht, andH. Ditlbacher, A. L. a. F. R. A. (2001). Optical properties of Ag and Au nanowire gratings*,* **90,** pp.
26. Flatau, B. T. D. a. P. J. *User Guide for the Discrete Dipole Approximation Code DDSCAT7.0, http://arxiv.org/pdf/0809.0337.pdf*.
27. Purcell, E. M. P., C. R. (1973). Scattering and Absorption of Light by Nonspherical Dielectric Grains*, Astrophysical Journal*, **186,** pp. 705-714.
28. Baffou, G., Girard, C., andQuidant, R. (2010). Mapping Heat Origin in Plasmonic Structures*, Physical Review Letters*, **104,** pp. 136805.
29. Baffou, G. andQuidant, R. (2013). Thermo-plasmonics: using metallic nanostructures as nano-sources of heat*, Laser & Photonics Reviews*, **7,** pp. 171-187.
30. Gotschy, W. (1996). Thin films by regular patterns of metal nanoparticles: Tailoring the optical properties by nanodesign*, Applied Physics B*, **63,** pp. 381-384.
31. Lowe, A. B. (2014). Thiol-ene "click" reactions and recent applications in polymer and materials synthesis: a first update*, Polymer Chemistry*, **5,** pp. 4820-4870.
32. Lowe, A. B. (2010). Thiol-ene "click" reactions and recent applications in polymer and materials synthesis*, Polymer Chemistry*, **1,** pp. 17-36.

33. Han, X., Wu, C., andSun, S. (2012). Photochemical reactions of thiol-terminated self-assembled monolayers (SAMs) for micropatterning of gold nanoparticles and controlled surface functionality*, Applied Surface Science*, **258,** pp. 5153-5156.
34. Lallana, E. (2012). Click Chemistry for Drug Delivery Nanosystems*, Pharmaceutical Research*, **29,** pp. 1-34.
35. Grand, J. (2005). Role of localized surface plasmons in surface-enhanced Raman scattering of shape-controlled metallic particles in regular arrays*, Physical Review B*, **72,** pp. 033407.
36. Grand, J. (2003). Optimization of SERS-active substrates for near-field Raman spectroscopy*, Synthetic Metals*, **139,** pp. 621-624.
37. Griesbaum, K. (1970). Problems and Possibilities of the Free-Radical Addition of Thiols to Unsaturated Compounds*, Angewandte Chemie International Edition in English*, **9,** pp. 273-287.
38. Dupin, D. (2007). Efficient Synthesis of Poly(2-vinylpyridine)−Silica Colloidal Nanocomposite Particles Using a Cationic Azo Initiator*, Langmuir*, **23,** pp. 11812-11818.
39. Northrop, B. H. andCoffey, R. N. (2012). Thiol–Ene Click Chemistry: Computational and Kinetic Analysis of the Influence of Alkene Functionality*, Journal of the American Chemical Society*, **134,** pp. 13804-13817.
40. Chi, Zhang, J., andUlstrup, J. (2006). Surface Microscopic Structure and Electrochemical Rectification of a Branched Alkanethiol Self-Assembled Monolayer*, The Journal of Physical Chemistry B*, **110,** pp. 1102-1106.
41. Kakiuchi, T. (2000). Phase Separation of Alkanethiol Self-Assembled Monolayers during the Replacement of Adsorbed Thiolates on Au(111) with Thiols in Solution*, Langmuir*, **16,** pp. 7238-7244.